

# Rovibrational Spectra for the HCCCN·HCN and HCN·HCCCN Binary Complexes in $^4\text{He}$ Droplets<sup>†</sup>

Francesco Paesani<sup>‡</sup> and K. Birgitta Whaley\*

Department of Chemistry and Pitzer Center for Theoretical Chemistry, University of California, Berkeley, California 94720

Gary E. Douberly<sup>§</sup> and Roger E. Miller

Department of Chemistry, University of North Carolina, Chapel Hill, North Carolina 27599

Received: March 15, 2007; In Final Form: May 18, 2007

Rovibrational spectra are measured for the HCCCN·HCN and HCN·HCCCN binary complexes in helium droplets at low temperature. Though no  $Q$ -branch is observed in the infrared spectrum of the linear HCN·HCCCN dimer, which is consistent with previous experimental results obtained for other linear molecules, a prominent  $Q$ -branch is found in the corresponding infrared spectrum of the HCCCN·HCN complex. This  $Q$ -branch, which is reminiscent of the spectrum of a parallel band of a prolate symmetric top, implies that some component of the total angular momentum is parallel to the molecular axis. The appearance of this particular spectroscopic feature is analyzed here in terms of a nonsuperfluid helium density induced by the molecular interactions. Finite temperature path integral Monte Carlo simulations are performed using potential energy surfaces calculated with second-order Möller–Plesset perturbation theory, to investigate the structural and superfluid properties of both HCCCN·HCN( $^4\text{He}$ ) $_N$  and HCN·HCCCN( $^4\text{He}$ ) $_N$  clusters with  $N \leq 200$ . Explicit calculation of local and global nonsuperfluid densities demonstrates that this difference in the rovibrational spectra of the HCCCN·HCN and HCN·HCCCN binary complexes in helium can be accounted for by local differences in the superfluid response to rotations about the molecular axis, i.e., different parallel nonsuperfluid densities. The parallel and perpendicular nonsuperfluid densities are found to be correlated with the locations and strengths of extrema in the dimer interaction potentials with helium, differences between which derive from the variable extent of polarization of the CN bond in cyanoacetylene and the hydrogen-bonded CH unit in the two isomers. Calculation of the corresponding helium moments of inertia and effective rotational constants of the binary complexes yields overall good agreement with the experimental values.

## I. Introduction

Helium ( $^4\text{He}$ ) nanodroplets at low temperatures have been shown to be a promising medium for assembling and studying atoms, molecules and clusters, some of which may not be formed by other means.<sup>1,2</sup> The weak interactions between helium and solutes, combined with the superfluid properties of the former, make these nanodroplets an almost ideal matrix for high-resolution spectroscopy. However, a comprehensive understanding of  $^4\text{He}$  superfluidity over microscopic length scales is needed to fully realize the capabilities of this approach.

Experiments on a large number of molecules dissolved in  $^4\text{He}$  at  $T \sim 0.37$  K have demonstrated that the vibrational spectra display the same fine structure (energy level patterns and selection rules) as the corresponding gas-phase molecules, which implies molecular free rotations accompanied by some renormalization of the rotational constant  $B$ .<sup>1,3–5</sup> In contrast, no fine structure was observed when the linear OCS molecule was solvated by fermionic  $^3\text{He}$  droplets (a normal fluid at  $T \sim 0.15$  K).<sup>6</sup> Experimental progress has recently allowed for the

observation of infrared and microwave spectra of dopant molecules also in small helium clusters as  $^4\text{He}$  atoms are added one by one.<sup>7–9</sup> On the theoretical side, quantum calculations of rotational excitations for several linear molecules in helium clusters have provided microscopic insight into the relationships between the underlying molecular interactions and the cluster structural properties.<sup>10–14</sup>

In this paper we report results for the experimental infrared spectra of the  $\nu_1$  (free) and  $\nu_2$  (hydrogen bonded) CH stretch bands of the linear HCCCN·HCN and HCN·HCCCN binary complexes in  $^4\text{He}$  droplets. Although no  $Q$ -branch is observed for the HCN·HCCCN dimer, which is consistent with previous experimental data obtained for other linear molecules,<sup>15,16</sup> a prominent  $Q$ -branch is found in the infrared spectrum of the HCCCN·HCN dimer. This  $Q$ -branch implies that there is a finite projection of the total angular momentum on the molecular axis and hence that some component of the total angular momentum is parallel to the molecular axis. In the gas phase, parallel vibrational bands of linear molecules that lack electronic angular momentum, such as the CH stretch of the linear HCCCN·HCN and HCN·HCCCN dimers, do not have angular momentum parallel to the molecular axis. Any angular momentum carried by helium can be quantified by the response to rotation of the boundaries, which determines the effective moment of inertia.<sup>17</sup> Even though, in the absence of vortices, no angular momentum

<sup>†</sup> Part of the “Roger E. Miller Memorial Issue”.

<sup>‡</sup> Current address: Center for Biophysical Modeling and Simulation, and Department of Chemistry, University of Utah, 315 S. 1400 E. Room 2020, Salt Lake City, UT 84112.

<sup>§</sup> Current address: Department of Chemistry, University of Georgia, Athens, GA 30602.

**TABLE 1: Parameters for the Lennard-Jones Potentials Used in the Fitting of the HCN·HCCCN–He and HCCCN·HCN–He Potential Energy Surfaces ( $\epsilon$  in  $\text{cm}^{-1}$ ,  $\sigma$  and  $z_i$  in  $\text{\AA}$ )**

	HCCCN·HCN–He					HCN·HCCCN–He				
	1	2	3	4	5	1	2	8	9	10
$\epsilon$	5.09389	8.80205	17.36540	13.32245	6.24281	6.43620	11.62391	14.37474	6.32450	9.65754
$\sigma$	3.41084	3.23165	3.17893	2.85302	3.55844	3.27258	3.43282	2.86972	3.45090	3.19154
$z_i$	−3.19038	−4.31343	0.39395	4.47296	3.32429	−2.74794	−0.53254	4.90422	3.65869	−3.88026

**TABLE 2: Molecular Constants Used in the Fitting and Simulation of the Spectra in Figures 1 and 2 (All in  $\text{cm}^{-1}$  unless Otherwise Noted)**

	HCCCN·HCN	HCCCN·HCN
$\nu_1$	3308.023	3324.127
$\Delta\nu_1$		+0.089
$\nu_2$	3259.333	3234.950
$\Delta\nu_2$		−4.063
$B''$	0.00760	0.00690
$B'$	0.00755	0.00685
$D'', D'$	$1 \times 10^{-6}$	$1 \times 10^{-6}$
$A'', A'$	0.6	0.015
$I_A$ ( $\text{amu}\cdot\text{\AA}^2$ )	28	1124
$I_B$ ( $\text{amu}\cdot\text{\AA}^2$ )	2218	2443
$\Delta I_B$ ( $\text{amu}\cdot\text{\AA}^2$ )	1060	980
$T$ (K)	0.37	0.37
$\gamma$ ( $\text{cm}^{-1}$ )	0.016 $\nu_1$ , 0.080 $\nu_2$	0.011 $\nu_1$ , 0.035 $\nu_2$
$B_{\text{gas}}/B_{\text{He}}$	3.1 (ab initio)	3.5

is allowed in a pure superfluid, the nonsuperfluid density induced by the molecular interaction around an embedded molecule can carry angular momentum.<sup>18,19</sup> The helium contribution to the moment of inertia tensor for a rotating molecule or complex can be evaluated by path integral Monte Carlo calculations.<sup>20</sup> We therefore complement the experimental measurements with finite temperature path integral Monte Carlo (PIMC) calculations to investigate the structural and superfluid properties of ( $^4\text{He}$ ) $_N$  clusters with  $N \leq 200$  containing either HCCCN·HCN or its isomer HCN·HCCCN, with the aim of elucidating the origin of the  $Q$ -branch and its sensitivity to the binary dimer structure. One of our primary motivations is to understand under what conditions a linear complex might show a spectroscopic  $Q$ -branch.

Recently, path integral Monte Carlo calculations for the  $\text{CO}_2(^4\text{He})_N$  clusters have demonstrated that the  $N$  dependence of measured effective rotational constants for small linear molecules can be quantitatively related to the size dependent superfluid response.<sup>21</sup> This analysis makes use of the linear response result that the superfluid response to rotation about an axis perpendicular to the molecular axis determines the helium contribution to the moment of inertia and, hence, in a local two-fluid analysis,<sup>18</sup> to the molecular rotational constant. In contrast, for all small linear molecules studied to date, the superfluid response to rotation about the molecular axis, termed the parallel response, has been found to be complete, consistent with experimental spectroscopic observations of linear rotor spectra (see below). For  $N$  less than the first molecular solvation shell, such calculations can be made with just the global superfluid fraction, but for  $N$  larger than one solvation shell, a consistent definition of the local superfluid response and corresponding superfluid and nonsuperfluid densities is required.<sup>22</sup> One earlier path integral analysis of a linear complex,  $(\text{HCN})_3$ , made with simple model interaction potentials claimed to find an incomplete average parallel superfluid response around the axis of the complex, but those calculations employed an inconsistent local superfluid estimator with correspondingly unreliable results.<sup>23</sup> In this work, we present the first calculations of the local parallel response around a linear complex in helium

droplets with a consistent local superfluid density estimator that can be quantitatively related to the rotational constants of the complex and use this to analyze the experimental infrared spectra of the two binary complexes of HCCCN with HCN.

The presence or absence of a  $Q$ -branch in the infrared spectrum of the two dimers is analyzed here in terms of the nonzero local parallel nonsuperfluid density that measures the response of the helium to rotations around the collinear molecular axes. The linear HCCCN·HCN dimer shows a region of significant parallel nonsuperfluid density at the hydrogen end of HCCCN, which results in an appreciable finite moment of inertia  $I_A$  along the HCCCN·HCN axis and appearance of a  $Q$ -branch in the simulated spectrum. The HCN·HCCCN isomer appears to show a very weak and significantly smaller parallel nonsuperfluid density near the nitrogen end of HCCCN and the resulting moment of inertia  $I_A$  along the HCN·HCCCN axis is too small to result in a visible  $Q$ -branch in the simulated spectrum. A similar trend, but to a lesser extent, is seen for the perpendicular nonsuperfluid densities, with the HCCCN·HCN dimer inducing a larger local perpendicular superfluid density and hence a somewhat larger moment of inertia  $I_B$ . Both of these results are consistent with the differences between the two dimers observed in the infrared spectra.

These differences in the local nonsuperfluid densities are analyzed here in the context of the corresponding interaction potentials of the dimers with helium and are seen to be correlated with the different locations and relative strengths of the various potential extrema. In particular, the HCCCN–HCN dimer has deeper global and first secondary minima in its interaction with helium, which causes greater perpendicular superfluid density in these locations. The origin of the differences in the parallel superfluid density is more subtle and shows correlations with the location of overlapping bands of helium density around the molecular axis that are located near the saddle points in the potential. The differences in these interaction potential features and hence the spectral differences between the two systems are assigned to differences in the polarization of the CN and hydrogen-bonded CH bonds in the two isomers. Although the accuracy of the current potential surfaces appears insufficient to obtain quantitative agreement of all moments of inertia with the values extracted from the experimental spectra, the infrared spectroscopic differences between the two dimers can nevertheless be clearly explained by the different distributions of local nonsuperfluid density around the dimers that derive from atomic scale differences in their interactions with helium.

## II. Methods

**A. Experimental Methods.** The experimental apparatus has been reviewed in detail.<sup>2</sup> Helium droplets are produced by expanding ultrahigh purity helium gas through a  $5 \mu\text{m}$  diameter nozzle cooled to 23 K with a closed cycle helium refrigerator (CTI-Cryogenics). The helium pressure behind the nozzle is 60 bar, and droplets with an average size of approximately 3000 helium atoms are produced. A 0.4 mm conical skimmer collimates the droplet beam 1 cm downstream from the nozzle.

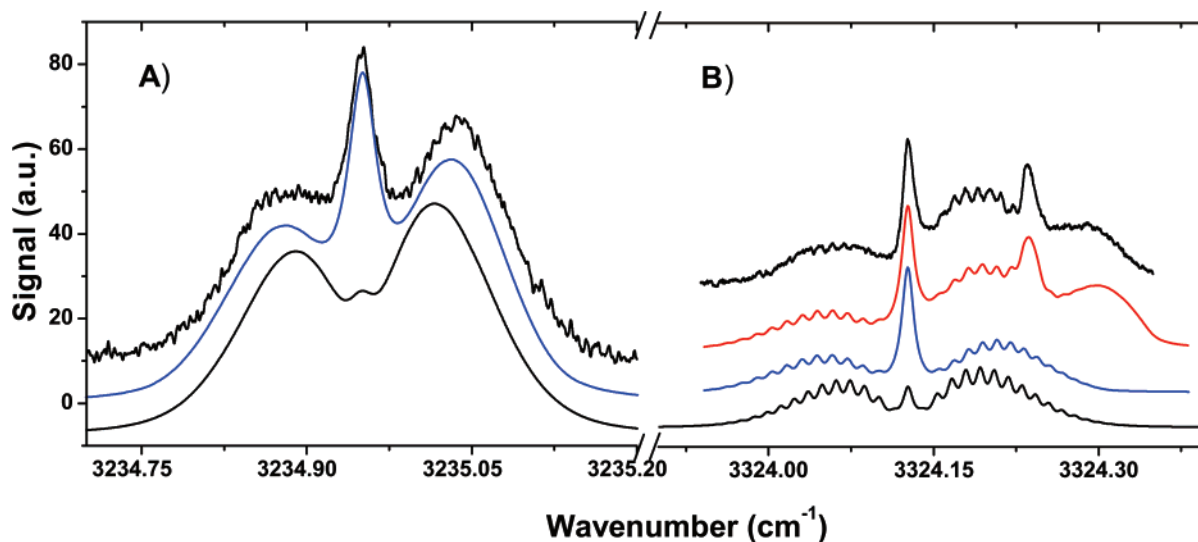


**Figure 1.** Rovibrational spectra of the (A)  $\nu_2$  and (B)  $\nu_1$  CH stretching fundamentals of the HCCCN·HCN complex. The spectrum in (B) is overlapped with the spectrum of the free CH stretching band of the HCCCN dimer. Shown below each experimental spectrum are simulations (blue) based on the constants in Table 2. Also shown is a simulation of the spectrum in (B) with the HCCCN dimer band included (red) (given the constants  $A = 0.0148 \text{ cm}^{-1}$ ,  $B'' = 0.0048 \text{ cm}^{-1}$ ,  $B' = 0.0047 \text{ cm}^{-1}$ , and a line width of  $0.018 \text{ cm}^{-1}$ ). Also shown (bottom, black) are the simulated spectra based on the theoretically determined effective moments of inertia about the  $A$  and  $B$  axis.

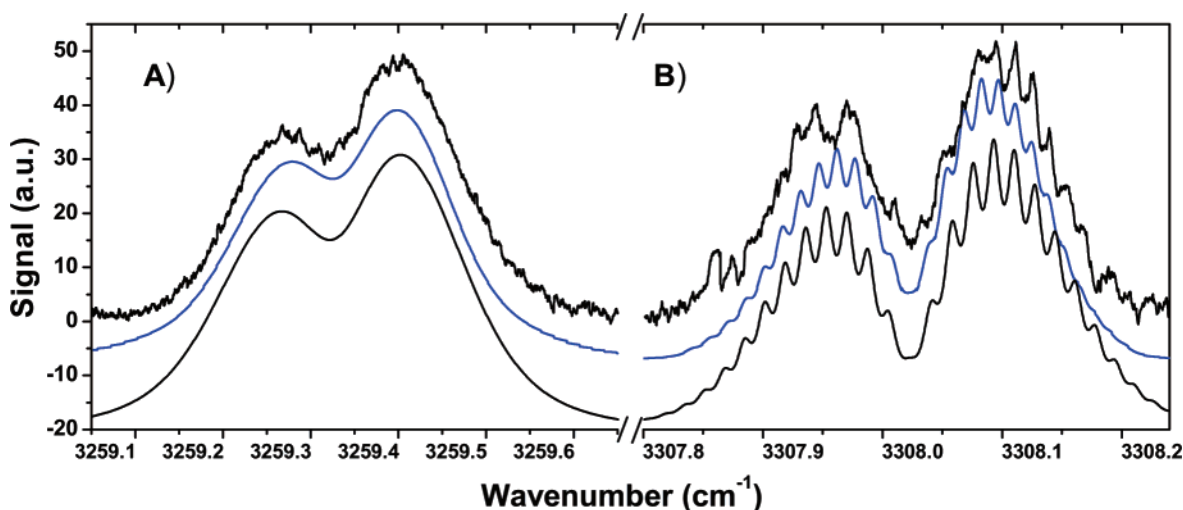


**Figure 2.** Rovibrational spectra of the (A)  $\nu_2$  and (B)  $\nu_1$  CH stretching fundamentals of the HCN·HCCCN complex. Shown below each spectrum are simulations (blue) based on the constants in Table 2. Also shown (bottom, black) are the simulated spectra based on the theoretically determined effective moments of inertia about the  $A$  and  $B$  axis.

The droplet beam passes through a 6 cm long differentially pumped gas pick-up cell containing both hydrogen cyanide (HCN) and cyanoacetylene (HCCCN), each having a partial pressure of  $4 \times 10^{-6}$  Torr. The partial pressures are optimized such that each droplet picks up on average one HCN and one HCCCN molecule. The translational and internal energy of each monomer, in addition to the condensation energy of the binary complex, is rapidly<sup>24</sup> removed by evaporative cooling of the droplet, resulting in a final temperature of 0.37 K.<sup>25</sup> Two parallel gold mirrors are used such that an F-center laser (Burleigh) operating on crystal #3 (RbCl:Li) can orthogonally intersect the droplet beam approximately 50 times. As the F-center laser is tuned into resonance with one of the CH stretch vibrations of either HCN·HCCCN or HCCCN·HCN, the excited vibrational energy is transferred to the droplet, resulting in the evaporation of approximately 600 helium atoms. The F-center laser is amplitude modulated, and the laser induced droplet beam depletion is monitored with a bolometer detector (Infrared Labs), using phase sensitive detection with a lock-in amplifier.

**B. Theoretical Methods.** Counterpoise corrected<sup>26</sup> potential energy surfaces (PESs) for both the HCN·HCCCN–He and HCCCN·HCN–He systems are computed using second-order Möller–Plesset perturbation theory with the atom-centered correlation-consistent double-zeta (aug-cc-pVDZ) basis set. The positions of both HCN·HCCCN and HCCCN·HCN dimers are fixed at their respective optimized geometries obtained at the same level of theory, and 1428 points are calculated for each system using Molpro.<sup>27</sup> These ab initio potential energy surfaces are significantly more realistic than that employed in an earlier PIMC study of the superfluid response around the HCN trimer.<sup>23</sup> The accuracy of the current surfaces was assessed by calculating a few points in regions of local minima with the more extensive aug-cc-pVTZ basis set. The locations of the minima were found to be unchanged, with only small differences of  $\sim 1.5 \text{ cm}^{-1}$  in the energies. We will show that this provides sufficient accuracy for the path integral analysis of the primary features of the experimental spectra, although a more accurate potential might

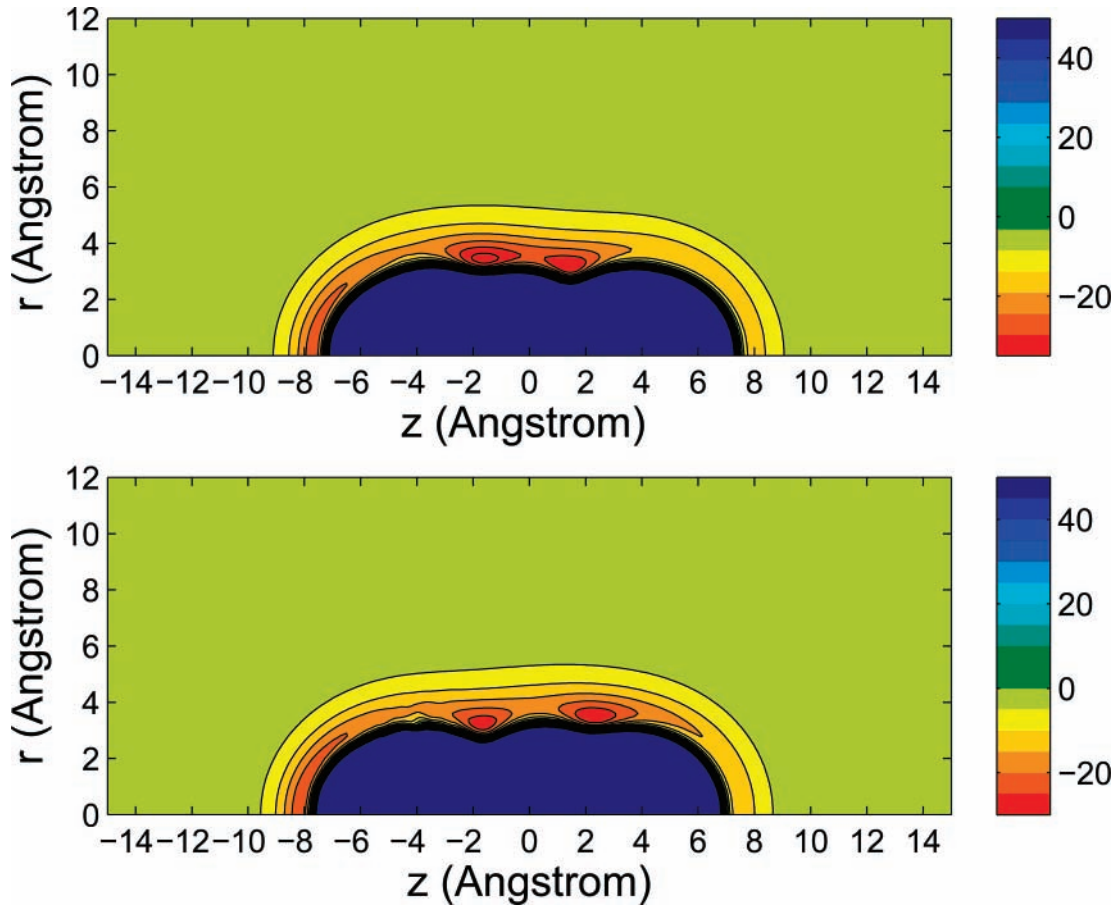


**Figure 3.** Contour plot of the HCCCN·HCN–He (top) and HCN·HCCCN–He (bottom) potential energy surfaces in cylindrical coordinates. Both HCCCN·HCN and HCN·HCCCN dimers lie on the  $z$ -axis. The atom coordinates in Å for the HCCCN·HCN dimer are  $z(\text{HCCCNHCN}) = -4.9839, -3.9081, -2.6723, -1.2883, -0.09760, +2.0750, +3.1595, +4.3426$ . The atom coordinates in Å for the HCN·HCCCN dimer are  $z(\text{HCNHCCCH}) = -5.4535, -4.3758, -3.1951, -1.0013, +0.08025, +1.3174, +2.7026, +3.8959$ . Energy in  $\text{cm}^{-1}$ . Color scale goes from red ( $-35.0 \text{ cm}^{-1}$ ) to blue ( $\geq 50.0 \text{ cm}^{-1}$ ).

allow full quantitative agreement with all moments of inertia components.

The total interaction potentials for both the HCN·HCCCN- $({}^4\text{He})_N$  and HCCCN·HCN- $({}^4\text{He})_N$  systems ( $N \leq 200$ ) are described as a sum of all pairwise contributions

$$V(\mathbf{R}) = \sum_{i=1}^N V^{\text{dimer-He}}(R_i, \vartheta_i) + \sum_{i<j}^N V^{\text{He-He}}(R_{ij}) \quad (1)$$

where  $R_{ij}$  is the distance between helium atoms  $i$  and  $j$ , and  $(R_i, \vartheta_i)$  are the Jacobi coordinates of the  $i$ th He in the center of mass frame of each specific dimer. For the helium–helium interaction  $V^{\text{He-He}}(R_{ij})$  the potential of ref 28 is used.

The structural and superfluid properties of the HCN·HCCCN- $({}^4\text{He})_N$  and HCCCN·HCN- $({}^4\text{He})_N$  systems at finite temperature are investigated using the path integral Monte Carlo method. This approach is based on Feynman's idea of mapping path integrals onto interacting classical ring polymers.<sup>29</sup> Because a detailed review of the method is given in ref 20 and its adaptation to molecule-doped helium clusters can be found in ref 30, only the details specific to the present study are discussed here.

In the PIMC scheme the thermal average of any local operator  $\hat{O}$  is given by

$$\langle \hat{O} \rangle = \frac{1}{Z} \int d\mathbf{R} d\mathbf{R}' \langle \mathbf{R}' | \hat{O} | \mathbf{R} \rangle \rho(\mathbf{R}, \mathbf{R}'; \beta) \quad (2)$$

where  $\beta = 1/k_B T$  and  $Z = \int d\mathbf{R} \rho(\mathbf{R}, \mathbf{R}; \beta)$  is the partition function. In eq 2  $\rho(\mathbf{R}, \mathbf{R}'; \beta)$  is the many-body density matrix at temperature  $T$ ,

$$\rho(\mathbf{R}, \mathbf{R}'; \beta) \equiv \langle \mathbf{R} | e^{-\beta \hat{H}} | \mathbf{R}' \rangle \quad (3)$$

where  $\hat{H}$  is the total Hamiltonian of the system. To incorporate the bosonic symmetry of the  ${}^4\text{He}$  atoms, the density matrix is symmetrized by summing over all permutations  $P$  among helium atoms,

$$\rho_B(\mathbf{R}, \mathbf{R}'; \beta) = \frac{1}{N!} \sum_P \rho(\mathbf{R}, P\mathbf{R}'; \beta) \quad (4)$$

Because the density matrix at low temperature is generally not known, in the path integral representation, it is replaced with a product of  $M$  higher-temperature density matrices:

$$\rho(\mathbf{R}, P\mathbf{R}'; \beta) = \int \dots \int d\mathbf{R}_1 d\mathbf{R}_2 \dots d\mathbf{R}_{M-1} \rho(\mathbf{R}, \mathbf{R}_1; \tau) \rho(\mathbf{R}_1, \mathbf{R}_2; \tau) \dots \rho(\mathbf{R}_{M-1}, P\mathbf{R}'; \tau) \quad (5)$$

where  $\tau = \beta/M$  is the imaginary time step defining the discrete representation of the path integral. At sufficiently high temperature  $MT$ , the density matrix can be approximated by a product of the free particle propagator and an interaction term,

$$\rho(\mathbf{R}, \mathbf{R}'; \tau) \approx \rho_0(\mathbf{R}, \mathbf{R}'; \tau) e^{-u(\mathbf{R}, \mathbf{R}'; \tau)} \quad (6)$$

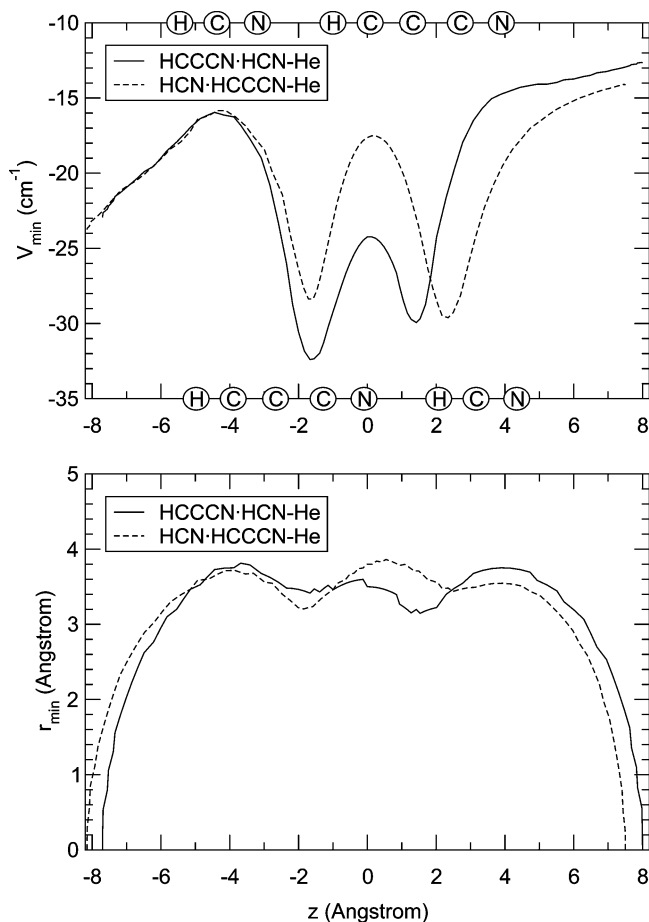


**Figure 4.** Minimum potential energy profile projected along the  $z$ -coordinate (top panel) and corresponding value of  $r = r_{\min}$  at the minimum potential point (bottom panel) for the HCCCN·HCN–He (solid line) and HCN·HCCCN–He (dashed line) potential energy surface.

**TABLE 3: Atomic Partial Charges ( $q$ ) for the HCCCN·HCN and HCN·HCCCN Binary Complex Obtained from the Corresponding Electrostatic Potentials**

	H	C	C	C	N	H	C	N
$q$	0.33	-0.25	-0.09	0.49	-0.47	0.29	0.08	-0.38
	H	C	N	H	C	C	C	N
$q$	0.28	0.09	-0.36	0.39	-0.34	-0.05	0.41	-0.43

In the case of the HCN·HCCCN( $^4\text{He}$ ) $_N$  and HCCCN·HCN( $^4\text{He}$ ) $_N$  systems, the interaction term  $e^{-u(\mathbf{R},\mathbf{R}';t)}$  is factorized into contributions deriving from the He–He and dimer–He interactions (with the dimer corresponding to either HCN·HCCCN or HCCCN·HCN),  $\rho^{\text{He-He}}$  and  $\rho^{\text{dimer-He}}$ , respectively. For the isotropic He–He potential,  $\rho^{\text{He-He}}$  is described by a pair-product of the exact two-body density matrices.<sup>20</sup> For the two anisotropic dimer–He interactions, the corresponding dimer–He potential energy surfaces are fitted to a sum of spherical interactions<sup>31,32</sup>

$$V^{\text{dimer-He}}(R,\vartheta) = \sum_k^K V_k(|\mathbf{R}-\mathbf{r}_k|) + \Delta V(R,\vartheta) \quad (7)$$

where  $V_k(|\mathbf{R}-\mathbf{r}_k|)$  is a Lennard-Jones potential with  $\mathbf{r}_k$  the position of the  $k$ th interaction site defining the zero in the radial coordinate for each  $V_k(|\mathbf{R}-\mathbf{r}_k|)$ . Symmetry considerations dictate that  $\mathbf{r}_k$  be located along the axis of each dimer, i.e.,  $\mathbf{r}_k = z_k$ . In eq 7  $\Delta V(R,\vartheta)$  is the “residual” potential energy surface necessary to reproduce the true dimer–He interactions. It has been

demonstrated that this approach greatly reduces the imaginary time step dependence of all the expectation values<sup>32</sup> because it allows the use of the exact two-body density matrix for each spherical interaction, whereas only the small contribution  $\Delta V(R,\vartheta)$  is treated within the less accurate “primitive approximation”.<sup>20</sup>

The number of Lennard-Jones potentials as well as their parameters are obtained from minimization of  $\Delta V(R,\vartheta)$  using the simulated annealing algorithm.<sup>33</sup> Five Lennard-Jones potentials are found to be sufficient to nearly completely reproduce the strength and anisotropy of both dimer–He interactions. The parameters  $\epsilon$ ,  $\sigma$ , and  $z_k$  for each of the five Lennard-Jones potentials for both the HCN·HCCCN–He and HCCCN·HCN–He systems are reported in Table 1.

All PIMC calculations are performed at a temperature  $T = 0.31$  K using the multilevel Metropolis algorithm,<sup>34</sup> with both HCN·HCCCN and HCCCN·HCN dimers fixed in space. Additional calculations carried out with translation and rotation of the dimers showed that the densities are essentially identical to those obtained with fixed dimers, as expected for molecular species significantly heavier than helium. This allows us to use the linear response formulation of the helium superfluid response which we now briefly summarize.

The path integral Monte Carlo method allows us to quantify the superfluidity of a bosonic system in terms of exchange-coupled paths that are comparable to the system size. Within the framework of the linear response theory, the global superfluid fraction,  $f_{\parallel(\perp)}^s$ , can be evaluated in terms of the projected area enclosed by the paths:<sup>20</sup>

$$f_{\parallel(\perp)}^s = \frac{4m^2 k_B T}{\hbar^2 I_{\parallel(\perp)}^{\text{cl}}} \langle A_{\parallel(\perp)} A_{\parallel(\perp)} \rangle \quad (8)$$

Here  $f_{\parallel(\perp)}^s$  quantifies the response of the  $^4\text{He}$  density to rotations around an axis parallel (perpendicular) to the axis of the dimer, with  $A_{\parallel(\perp)}$  the area of a path projected into a plane perpendicular (parallel) to the same axis, and  $I_{\parallel(\perp)}^{\text{cl}}$  the corresponding classical moment of inertia. Using the  $I$ -normalized estimator of the local superfluid response,<sup>22</sup> the local superfluid densities are computed as

$$\rho^s(\mathbf{R})_{\parallel(\perp)} = \frac{4mk_B T \langle A_{\parallel(\perp)} A_{\parallel(\perp)}(\mathbf{R}) \rangle}{\hbar^2 r^2} \quad (9)$$

where

$$A_{\parallel(\perp)}(\mathbf{R}) = \frac{1}{2} \sum_{i=1}^N \sum_{k=1}^M (\mathbf{r}_{i,k} \times \mathbf{r}_{i,k+1})_{\parallel(\perp)} \delta(\mathbf{R}-\mathbf{r}_{i,k}) \quad (10)$$

$M$  is the number of time slices in the discrete path integral representation,<sup>20</sup> and  $A_{\parallel(\perp)}(\mathbf{R})$  is the sum of all area segments passing through the differential volume  $d^3\mathbf{R}$  and thus represents the local contribution of all paths to the projected area  $A_{\parallel(\perp)}$ . The local nonsuperfluid densities  $\rho_{\parallel(\perp)}^{\text{ns}}(\mathbf{R})$  are then obtained from

$$\rho_{\parallel(\perp)}^{\text{ns}}(\mathbf{R}) = \rho(\mathbf{R}) - \rho_{\parallel(\perp)}^s(\mathbf{R}) \quad (11)$$

where  $\rho(\mathbf{R})$  is the total helium density and  $\rho^s(\mathbf{R})$  is the parallel (perpendicular) density defined in eq 9. The helium contributions to the principal moments of inertia  $I_\alpha$  are obtained within a local two-fluid description from integration of the nonsuperfluid densities according to<sup>22</sup>

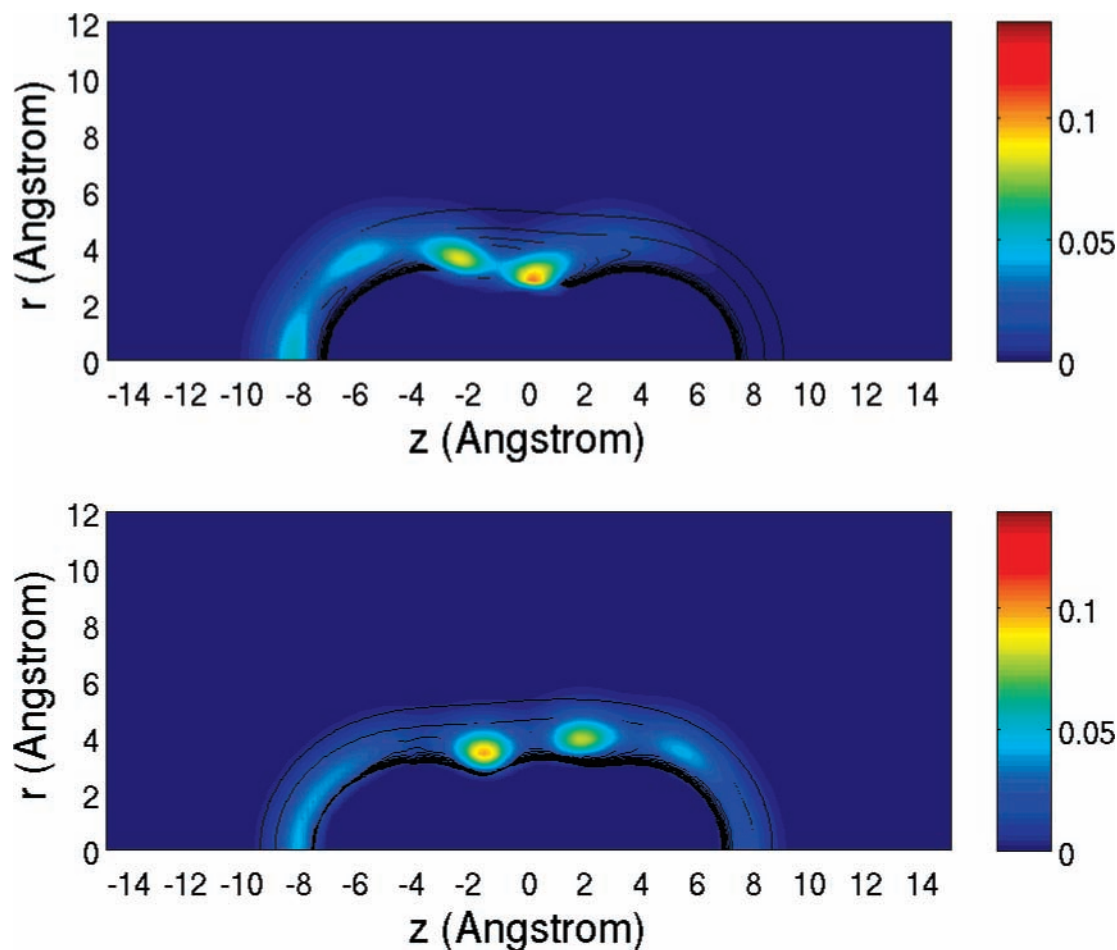


**Figure 5.**  $^4\text{He}$  total density distribution for the HCCCN•HCN( $^4\text{He}$ ) $_N$  (top) and HCN•HCCCN( $^4\text{He}$ ) $_N$  (bottom) systems with  $N = 20$ . See Figures 3 and 4 for the locations of the HCN and HCCCN units.

$$I_\alpha = m \int [\rho(\mathbf{R}) - \rho_\alpha^s(\mathbf{R})] R_\perp^2 d^3\mathbf{R} \quad (12)$$

with  $R_\perp$  the distance from the principal axis  $\hat{x}_\alpha$ . For a linear dimer complex,  $\alpha$  takes two values  $\parallel$  and  $\perp$ , corresponding to principal axes parallel and perpendicular to the (collinear) molecular axes, respectively.

### III. Results

The experimental spectra of the  $\nu_1$  and  $\nu_2$  CH stretch bands of the HCCCN•HCN and HCN•HCCCN dimers are shown at the top of Figures 1 and 2, respectively. The  $\nu_1$  spectrum of HCCCN•HCN in Figure 1B is overlapped with the free CH stretching band of the HCCCN•HCCCN dimer. As observed previously for the helium solvated linear HCN•HCN dimer,<sup>35</sup> the free ( $\nu_1$ ) CH stretch spectra have narrower line widths than the corresponding bonded ( $\nu_2$ ) CH stretch spectra. The same trend is observed in the gas phase<sup>36,37</sup> and is well-known<sup>38</sup> to occur due to the stronger coupling of the bonded CH stretch to the dimer dissociation coordinate, leading to a shorter vibrational predissociation lifetime, in comparison to the free stretch. A correspondence between the vibrational predissociation lifetimes in the gas phase and the line widths measured for the same complexes solvated in helium droplets has been observed now on several occasions.<sup>2</sup>

Comparing the  $\nu_1$  and  $\nu_2$  band origins of the HCCCN•HCN isomer to the gas-phase values, we observe solvent shifts of  $0.089 \text{ cm}^{-1}$  to the blue and  $4.063 \text{ cm}^{-1}$  to the red, respectively. These solvent frequency shifts are comparable in magnitude to those observed previously for the linear HCN•HCN<sup>35</sup> and

HCCCN•HCCCN<sup>39</sup> dimers. Although the small magnitude of these frequency shifts from the gas-phase band origins<sup>36,37</sup> provide considerable support to the assignment of the vibrational bands in Figure 1 to a linear HCCCN•HCN dimer, the rotational structure of the spectra certainly does not resemble that of a linear molecule. The prominent  $Q$ -branch is instead reminiscent of the spectrum of a parallel band of a prolate symmetric top. Nevertheless, the only structures that are minima on the HCCCN/HCN intermolecular potential energy surface are the two linear dimer configurations, and the intermolecular potential is strongly anisotropic with respect to the dimer bending coordinate.<sup>40</sup> Additionally, if the helium solvated HCCCN•HCN dimer were nonlinear, we would have instead expected a blue shift of the hydrogen-bonded CH stretch from the  $\nu_2$  vibrational band origin of the linear structure observed in the gas phase. When the complex bends, the HC bond length decreases, increasing its frequency and hence inducing a blue shift relative to its value in the gas-phase complex. Though this might be partially compensated in the helium droplet by a solvent shift contribution to the red, the relatively large overall red shift of the  $\nu_2$  mode indicates that the dipole induced polarization of the solvent is maximized in the linear configuration. Similar arguments can be made to provide additional support of the assignment of the HCN–HCCCN complex to a linear structure.

We note that the presence of a  $Q$ -branch in the spectrum of a linear complex embedded in helium droplets is not without precedent. In fact, the first such observation was for the spectrum of the linear HCCCN•HCCCN dimer,<sup>39</sup> as can be seen in Figure 1B centered at  $3324.24 \text{ cm}^{-1}$ . The spectra of the linear (HCN) $_n$

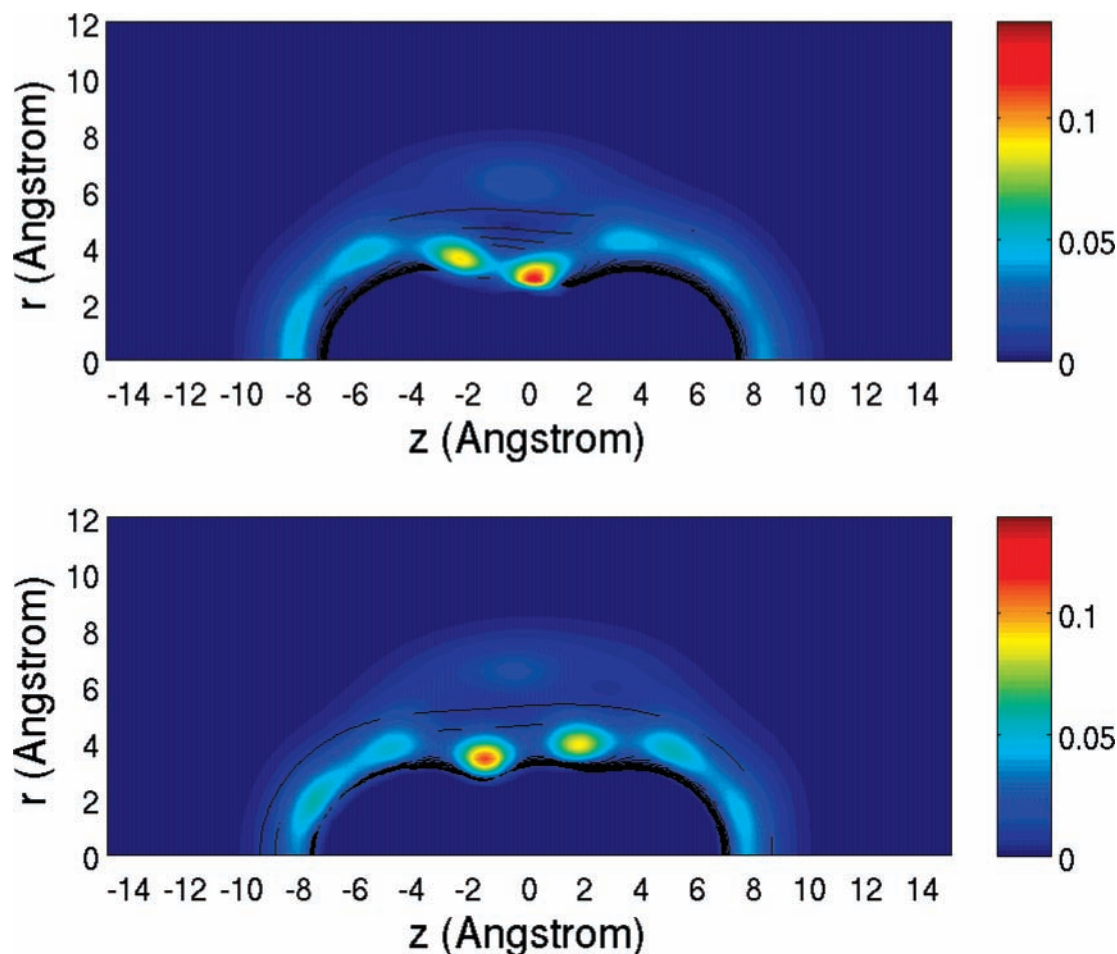


**Figure 6.**  $^4\text{He}$  total density distribution for the  $\text{HCCCN}\cdot\text{HCN}(^4\text{He})_N$  (top) and  $\text{HCN}\cdot\text{HCCCN}(^4\text{He})_N$  (bottom) systems with  $N = 40$ . See Figures 3 and 4 for the locations of the HCN and HCCCN units.

chains<sup>41</sup> also possess an anomalous  $Q$ -branch for  $n \geq 3$  (but not for  $n = 2$ ).<sup>42</sup> Although  $Q$ -branches were also seen in the spectra of the linear OCS molecule when complexed with variable numbers of  $\text{H}_2$  and  $\text{D}_2$  molecules in helium droplets,<sup>43</sup> the resulting complexes are not linear and thus the presence of a  $Q$ -branch in those systems is not surprising.

Below each spectrum in Figure 1 is a simulation (blue curve) of the experimental spectra with use of a prolate symmetric top Hamiltonian whose constants are summarized in Table 2. In these spectral simulations the temperature is fixed to 0.37 K,<sup>25</sup> and all rotational constants are obtained by fitting the spectrum for  $\nu_1$  only (Figure 1B). These rotational constants are then used with a variable Lorentzian line width to make the simulation of the  $\nu_2$  stretch spectrum shown in Figure 1A.

The  $A$  constant required to fit the intensity of the  $Q$ -branch of the free CH stretch in the HCCCN·HCN isomer corresponds to a moment of inertia about the  $A$ -axis equal to  $1124 \text{ amu } \text{\AA}^2$  (Table 2). In addition, we find that the  $B$  rotational constant has been reduced by a factor of 3.5 from the gas-phase value,<sup>36,37</sup> corresponding to an increase in  $I_B$  equal to  $980 \text{ amu } \text{\AA}^2$ . A factor of approximately 3 reduction in the  $B$  rotational constant is typical of what has been observed previously for heavier molecular complexes solvated in helium droplets.<sup>15,16,25</sup> The corresponding values for the HCN·HCCCN isomer summarized in Table 2 show a similar reduction in the  $B$  rotational constant, compared in this case to the ab initio value obtained from the optimized equilibrium geometry, because a gas-phase value has not been reported. This is not surprising given the similar lengths of the two isomers; however, it is interesting that the prominent

$Q$ -branch observed for the other isomer is absent here. In fact, the moment of inertia about the  $A$ -axis of HCN·HCCCN must be at least  $1100 \text{ amu } \text{\AA}^2$  smaller than that for the HCCCN·HCN isomer, given that a  $Q$ -branch is absent from the simulation in Figure 2B for all values of the  $A$  rotational constant greater than  $0.6 \text{ cm}^{-1}$ .

The differences between the spectra of the HCN·HCCCN and HCCCN·HCN complexes in helium are now analyzed in terms of the  $^4\text{He}$  density distribution and  $^4\text{He}$  superfluidity by performing path integral Monte Carlo calculations at  $T = 0.31 \text{ K}$  for the HCN·HCCCN( $^4\text{He}$ ) $_N$  and HCCCN·HCN( $^4\text{He}$ ) $_N$  systems with  $N \leq 200$ , using the total interaction potentials of eq 1. The potential energy surfaces for the HCN·HCCCN–He and HCCCN·HCN–He systems in cylindrical coordinates are shown in Figure 3, respectively. Both the interactions display very similar features, with the HCCCN·HCN–He potential being overall slightly more attractive. For the HCCCN·HCN–He system the global minimum of  $-32.4 \text{ cm}^{-1}$  is located at  $z = -1.67 \text{ \AA}$ ,  $r = 3.41 \text{ \AA}$ , near the single C–C bond of cyanoacetylene. Two other local minima are found. The first, with energy  $-29.9 \text{ cm}^{-1}$ , is located at  $z = 1.42 \text{ \AA}$ ,  $r = 3.20 \text{ \AA}$ , near the hydrogen-bonded H of HCN, and the second has energy  $-22.93 \text{ cm}^{-1}$  and is located at  $z = -7.70 \text{ \AA}$ ,  $r = 0.00 \text{ \AA}$ , corresponding to the linear geometry He–HCCCN·HCN. The global minimum of the HCN·HCCCN–He potential energy surface is somewhat higher in energy,  $-29.6 \text{ cm}^{-1}$ , and is also located near the single C–C bond of cyanoacetylene, at  $z = 2.35 \text{ \AA}$ ,  $r = 3.48 \text{ \AA}$ . The first local minimum has a well depth of  $-28.4 \text{ cm}^{-1}$  and is found at  $z = -1.58 \text{ \AA}$ ,  $r = 3.23 \text{ \AA}$ , near the  $\text{C}\equiv\text{C}$  triple bond,

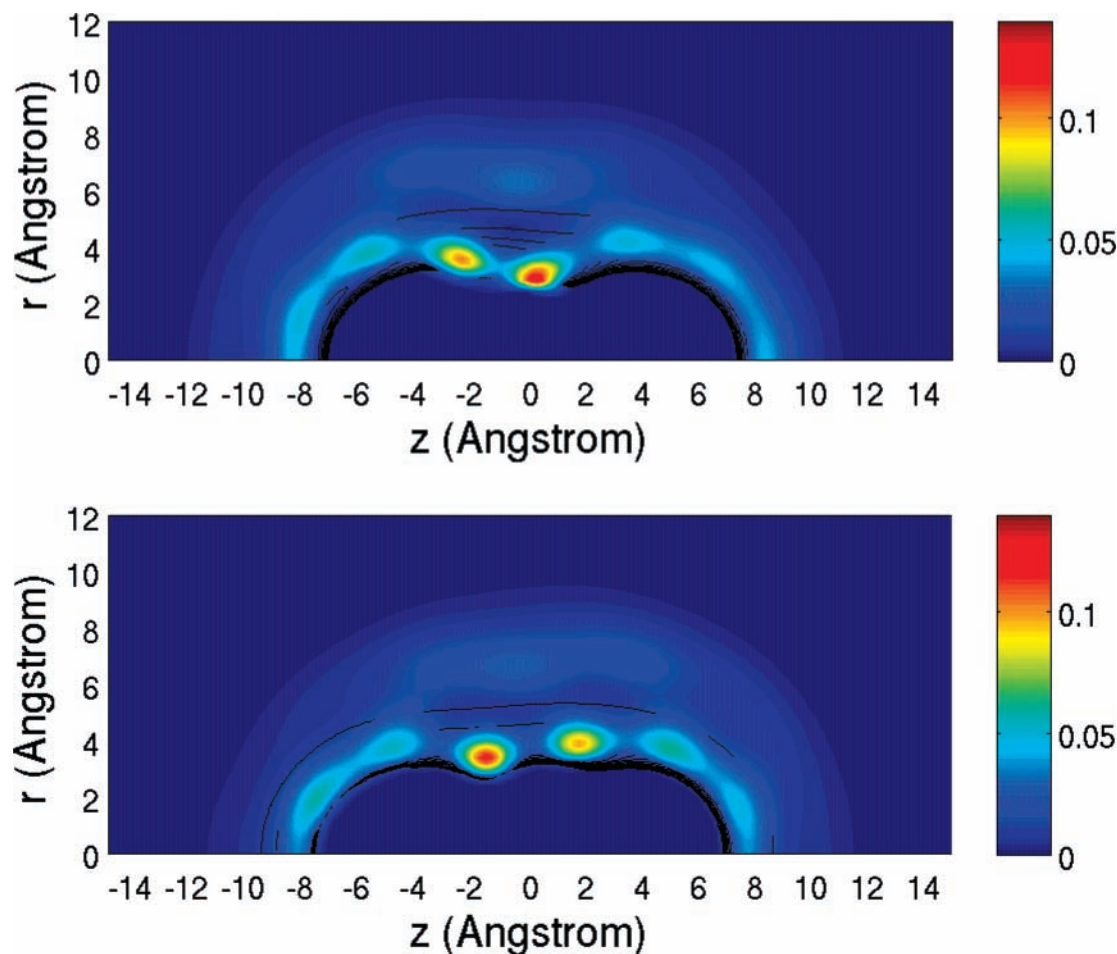


**Figure 7.**  $^4\text{He}$  total density distribution for the HCCCN·HCN( $^4\text{He}$ ) $_N$  (top) and HCN·HCCCN( $^4\text{He}$ ) $_N$  (bottom) systems with  $N = 60$ . See Figures 3 and 4 for the locations of the HCN and HCCCN units.

and the second local minimum of  $-23.74\text{ cm}^{-1}$  is located at  $z = -8.15\text{ \AA}$ ,  $r = 0.00\text{ \AA}$ , corresponding to the linear geometry He–HCN·HCCCN. The location of the global minima near the single C–C bond of cyanoacetylene for both complexes is consistent with the greater binding of helium to cyanoacetylene than to HCN (well depths  $\sim 40\text{ cm}^{-1}$ <sup>44</sup> and  $\sim 26\text{ cm}^{-1}$ ,<sup>45</sup> respectively) and with the T-shaped geometry of the global minimum for He–HCCCN<sup>44</sup> and complexes of cyanoacetylene with electronegative atoms such as Mg.<sup>46</sup> As noted earlier, carrying out the ab initio calculations at a higher level of accuracy introduces small changes in the energetics but does not change the locations of the potential minima.

We can further analyze the preferential localization of helium atoms around the two isomers in terms of the molecular electron density by making use of the atomic partial charges. These are fitted for all atoms to the corresponding electrostatic potentials, and the resulting values are summarized in Table 3 for both dimer complexes with helium. These partial charges show that although the C≡C triple bond carbon atoms are strongly negatively polarized, the adjacent C and H atoms are in all cases positively polarized. The helium atom prefers to sit in a region of partial positive polarization, explaining the location of the global and local minima in the potentials of Figure 3.

Table 3 further reveals quantitative differences between the partial charge distribution along the dimer axis that account for the detailed differences between the two dimer interactions with helium, as we now show. Some critical differences between the HCN·HCCCN–He and HCCCN·HCN–He potential energy surfaces become more evident when the minimum potential

energy profiles are analyzed. These are shown as projections on the  $z$ -coordinate in the top panel of Figure 4. The two interactions are nearly identical when the He atom approaches the H-end of each dimer ( $z > 0.0$ ,  $r = 0.0$ ). They are also very similar for the opposite linear geometry with the He atom approaching the N-end of each dimer ( $z < 0.0$ ,  $r = 0.0$ ). In contrast, the more attractive regions near  $z \approx 0.0\text{ \AA}$  appear quite different in the two cases. In particular, the global minimum is higher for HCN·HCCCN–He and the barrier separating the global and first local minima is significantly higher for this system. This reflects the longer region of negative polarization over the C≡C triple bond of HCCCN with this dimer, whereas with the other species, HCCCN·HCN, the large negative polarization at the N atom in HCCCN is offset by strong positive polarizations of the adjacent C and H atoms. This results in an attractive polarization gradient for helium in both directions along the molecular axis at this location and, consequently, in a lower barrier for the HCCCN·HCN dimer. For the second saddle point, located at  $z \sim -4\text{ \AA}$  and  $r \sim 3.6\text{ \AA}$ , more subtle features are also of interest. The bottom panel of Figure 4 shows the corresponding value of  $r = r_{\text{min}}$  at the minimum potential point as a function of  $z$ . We see that although the second saddle point has a similar location and magnitude for both isomers, the distance of this from the nearest minimum to the right is noticeably different, with latter occurring at  $r = 3.23\text{ \AA}$  for HCCCN–HCN (first secondary minimum) and at  $r = 3.41\text{ \AA}$  for HCN–HCCCN (global minimum). Therefore, the distance between the saddle point and nearest minimum is greater for the HCN–HCCCN isomer and, consequently, we expect that

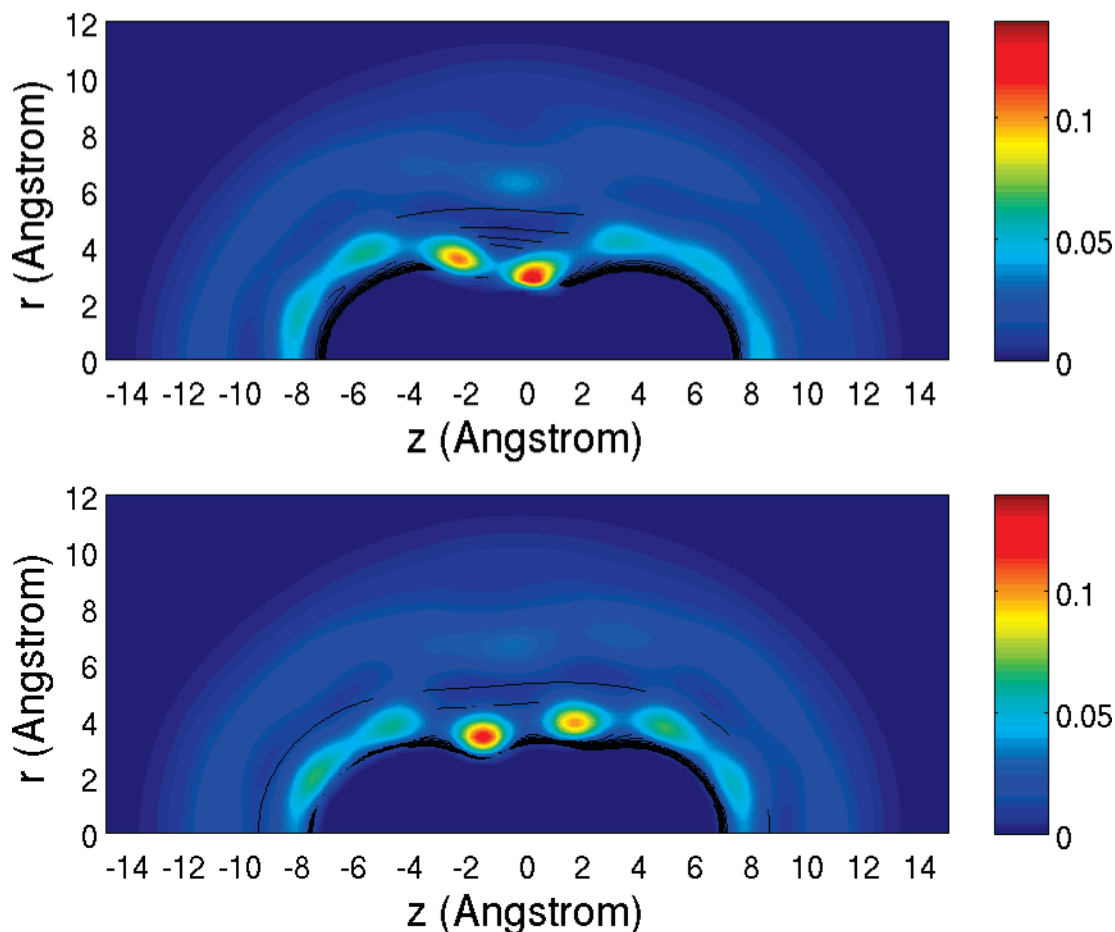


**Figure 8.**  $^4\text{He}$  total density distribution for the HCCCN·HCN( $^4\text{He}$ ) $_N$  (top) and HCN·HCCCN( $^4\text{He}$ ) $_N$  (bottom) systems with  $N = 100$ . See Figures 3 and 4 for the locations of the HCN and HCCCN units.

more helium atoms will be located between these two potential extrema. In addition, we also notice that the  $r$ -gradient in the minimum potential to the left of the minimum is greater for HCCCN–HCN.

The helium density distributions for the HCN·HCCCN( $^4\text{He}$ ) $_N$  and HCCCN·HCN( $^4\text{He}$ ) $_N$  systems with  $N = 20, 40, 60, 100$ , and 200 computed at temperature  $T = 0.31$  K are compared in Figures 5–9, respectively. Clearly, as expected, the  $^4\text{He}$  atoms are preferentially located in the regions where the underlying interaction is stronger. Thus, in both cases the two regions of higher helium density correspond to the global and first local minima, near the regions of greatest positive charge on the molecular axis. We note that for both species the maximum density is found in the first local minimum, rather than in the global minimum. This is due to the larger spatial extent of the first local minimum (Figure 3) and emphasizes the importance of the multidimensional nature of the potential energy surface. It is also interesting to note that although the HCN·HCCCN dimer is completely solvated at  $N = 20$ , a larger number of He atoms is necessary to close the first solvation shell in the case of the HCCCN·HCN dimer. This is consistent with the greater binding He to the HCCCN·HCN dimer. A second solvation shell starts forming at  $N \approx 30$ –40, and a third solvation shell appears at  $N \approx 200$ . Overall, the He density distributions for the less strongly bound HCN·HCCCN( $^4\text{He}$ ) $_N$  system appear to be slightly more localized along the molecular axes, particularly in the first solvation shell. This increased angular localization reflects the greater barrier in the minimum energy profile, Figure 4.

Given the high computational cost required for calculation of superfluid properties, the analysis of the superfluid fractions and densities is performed here only for  $N \leq 100$ . The global superfluid fractions for the HCN·HCCCN( $^4\text{He}$ ) $_N$  and HCCCN·HCN( $^4\text{He}$ ) $_N$  systems as a function of  $N$  are reported in Table 4. For both isomers the parallel superfluid fraction is larger than the perpendicular fraction, with a value increasing slightly with  $N$  and close to 1.0 for all sizes. In contrast, the perpendicular fraction increases as a function of  $N$ , approaching 1.0 only at  $N = 100$ . The global superfluid fraction represents the superfluid response averaged over all homogeneous and inhomogeneous regions of a system and consequently, it does not provide any insight into the local distribution of the superfluid density or into the helium contribution to the moment of inertia that derives from a weighted integration of the complementary nonsuperfluid density (eq 12). Thus, although the size dependence of the parallel fraction does imply some parallel nonsuperfluid density in the first solvation shell, one cannot extract any detailed information on the contributions to the effective molecular moments of inertia from this function. For a microscopic understanding of the difference in moments of inertia of the two species, we therefore have to analyze the local superfluid densities derived from the  $I$ -normalized estimator.<sup>22</sup> Figures 10 and 11 show the perpendicular and parallel nonsuperfluid densities, respectively (eq 11), for both the HCN·HCCCN( $^4\text{He}$ ) $_N$  and HCCCN·HCN( $^4\text{He}$ ) $_N$  systems with  $N = 100$ . The corresponding  $^4\text{He}$  contributions to the effective moments of inertia  $I_{A(B)}$  obtained from the integration of  $\rho_{||(\perp)}^{\text{ns}}(\mathbf{R})$  are reported in Table 5. For both systems, the moment of inertia

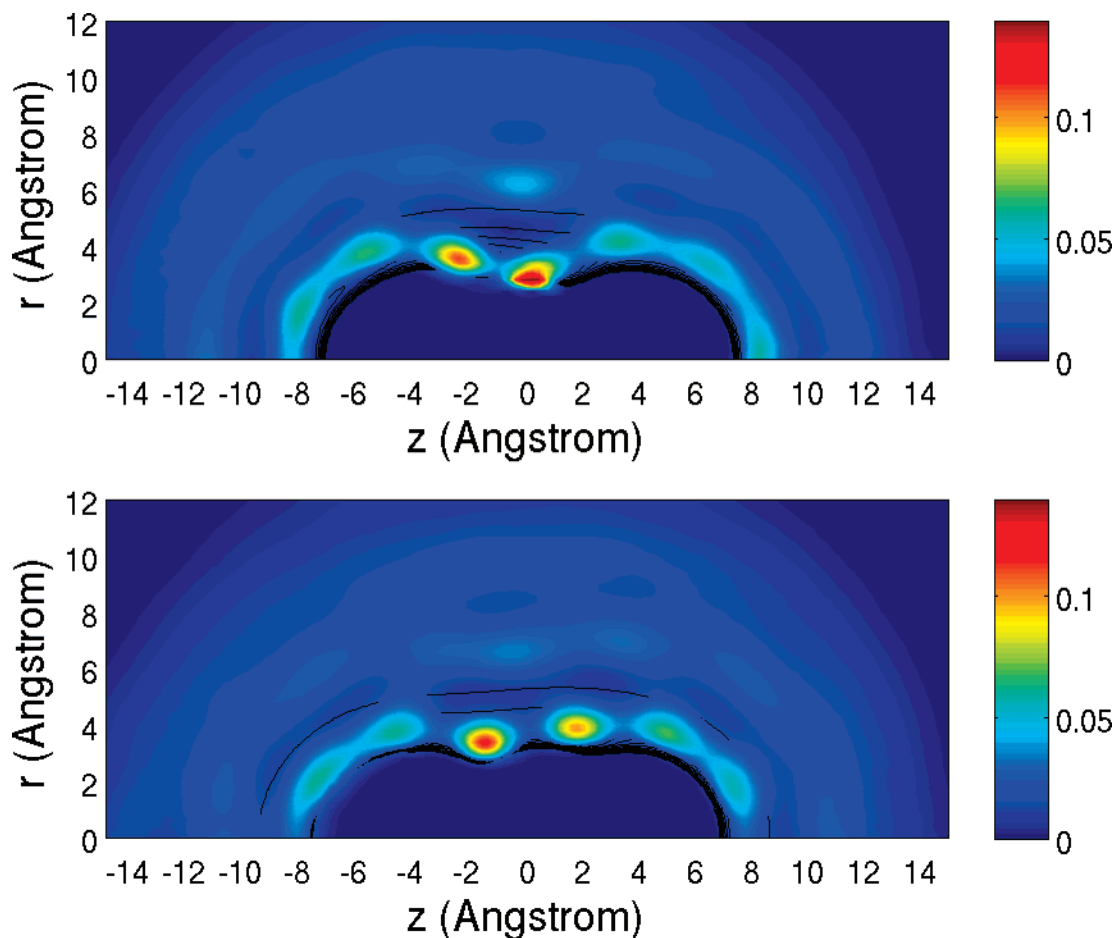


**Figure 9.**  $^4\text{He}$  total density distribution for the HCCCN·HCN( $^4\text{He}$ ) $_N$  (top) and HCN·HCCCN( $^4\text{He}$ ) $_N$  (bottom) systems with  $N = 200$ . See Figures 3 and 4 for the locations of the HCN and HCCCN units.

**TABLE 4: Superfluid Fractions  $f_{\parallel(\perp)}^s$ , Eq 8, for HCCCN·HCN( $^4\text{He}$ ) $_N$  and HCN·HCCCN ( $^4\text{He}$ ) $_N$  Systems with  $N < 100^a$**

		$N = 20$	$N = 40$	$N = 60$	$N = 100$
$f_{\parallel}^s$	HCCCN·HCN( $\text{He}$ ) $_N$	0.92(1)	0.96(1)	0.98(1)	0.98(1)
	HCN·HCCCN( $\text{He}$ ) $_N$	0.93(1)	0.96(1)	0.99(1)	0.99(1)
$f_{\perp}^s$	HCCCN·HCN( $\text{He}$ ) $_N$	0.50(1)	0.77(1)	0.87(1)	0.92(1)
	HCN·HCCCN( $\text{He}$ ) $_N$	0.52(1)	0.78(1)	0.87(1)	0.95(1)

<sup>a</sup> Numbers in parentheses correspond to the statistical uncertainty in units of the last digit.

contribution was evaluated by taking into account only contributions from the first solvation shell. This choice is justified by the fact that (1) the inspection of the total density shows that the number of helium atoms ( $N_{1st} \approx 30-35$ ) as well as their spatial distribution in the first solvation shell remain essentially unchanged going from  $N = 100$  to  $N = 200$  and (2) the helium density in the outer shells is found to be completely superfluid within the statistical error of the calculations.

A nonzero perpendicular nonsuperfluid  $^4\text{He}$  density is found in the first solvation shell for both systems, resulting in  $^4\text{He}$  contributions (Table 5) to the effective moments of inertia  $I_B$  in very good agreement with the values estimated from simulations of the corresponding experimental spectra (bottom line of Table 2). The resulting theoretical rotational constant  $B$  is found to be reduced by a factor of about 3, just as deduced from the experimental results (the theoretical  $B$  value corresponds to the experimental  $B''$  value). Furthermore, the moment of inertia increment is seen to be  $\sim 30\%$  less for the HCN·HCCCN dimer, in fair agreement with the relative reduction of

$\sim 10\%$  seen in experiment. The larger value of  $\Delta I_B = I_B - I_B^{\text{dimer}}$  for HCCCN–HCN derives from a larger perpendicular nonsuperfluid density that is due to the larger binding of helium in the global and first secondary maxima for this isomer (see Figures 3 and 4), which lowers the propensity for helium in these locations to undergo exchange with helium at different  $z$  values.

A similar general trend is seen for the parallel nonsuperfluid densities and moments of inertia, although detailed interpretation of the difference between the two isomers is not as clear in this case. Thus the parallel nonsuperfluid density computed for the HCCCN·HCN( $^4\text{He}$ ) $_{100}$  cluster is significantly larger than the corresponding density for the HCN·HCCCN( $^4\text{He}$ ) $_{100}$  cluster (Figure 11). For the latter isomer the nonsuperfluid density is very weak and diffuse, preventing a definitive analysis of its distribution around the molecule although it is apparent that the only region of noticeable density is at the end of the HCCCN moiety, in a region approaching a maximum in the potential energy. For the other isomer, HCCCN·HCN, the parallel nonsuperfluid density is located near the free CH unit of cyanoacetylene, in the region of the second local minimum of the potential energy surface. Inspection of the total densities (Figure 8) shows that the helium density in this region is quite similar for the two isomers, with the density around HCN–HCCCN showing slightly more localized bands. It is not immediately obvious why permutation rings encircling the molecular axis are preferentially suppressed for HCCCN–HCN in this region. One possibility is that because the density profile as a function of  $r$  is smoother, there is a greater propensity for atoms to exchange in the radial direction so that the contribution

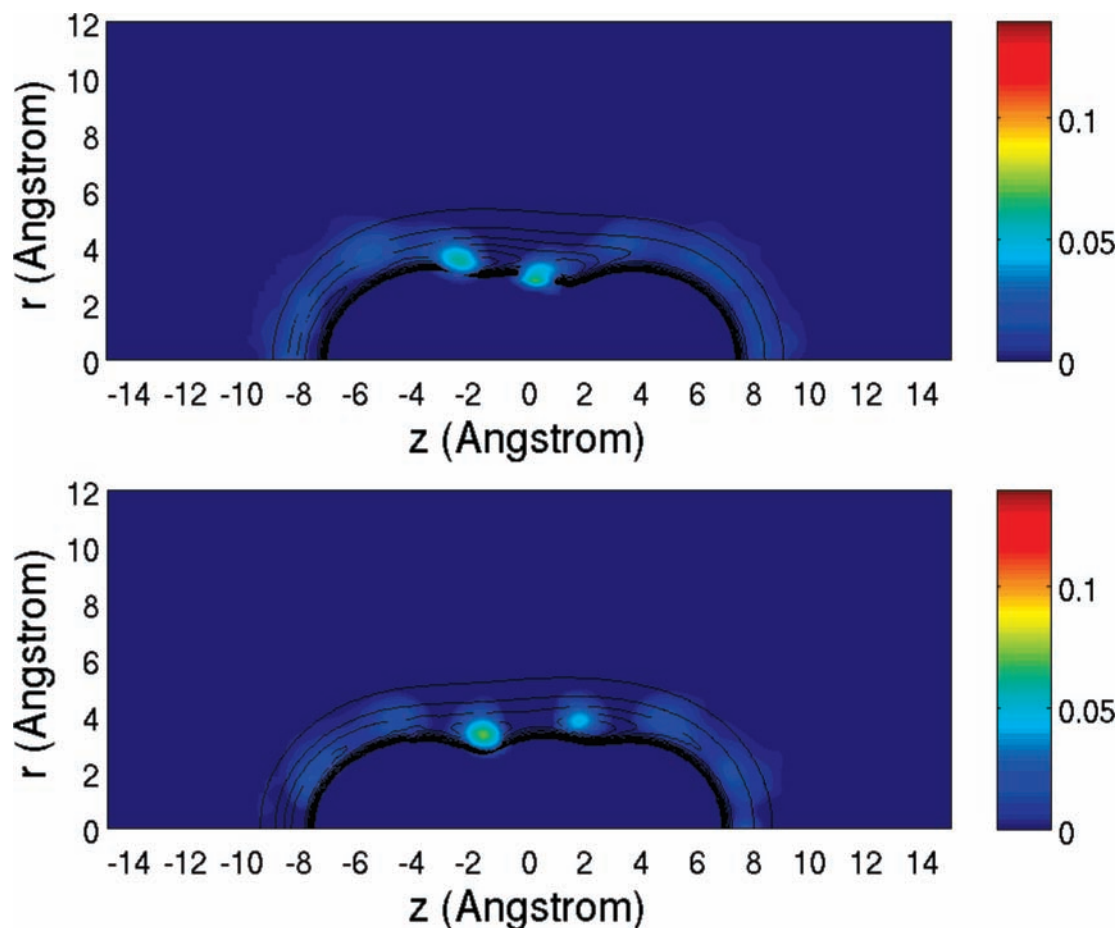


**Figure 10.**  $^4\text{He}$  perpendicular superfluid density for the  $\text{HCCCN}\cdot\text{HCN}(^4\text{He})_N$  (top) and  $\text{HCN}\cdot\text{HCCCN}(^4\text{He})_N$  (bottom) systems with  $N = 100$ .

to the projected area  $A_{\parallel}(\mathbf{R})$  (eq 10) is reduced. Both the helium–helium interactions and the gradient of the potential energy profile are involved in determining the density profile and the propensity to undergo permutation exchanges. Achieving a full understanding of the difference in permutation exchanges contributing to parallel superfluidity in a region of small differential densities like this negative  $z$  region will require a more detailed analysis of the exchange paths in the two systems. On integration of the parallel nonsuperfluid density according to ref 22, we find that the  $^4\text{He}$  contribution to the effective moment of inertia  $\Delta I_A = I_A - I_A^{\text{dimer}} = I_A$  (assuming the linear structure of the dimer, so that  $I_A^{\text{dimer}} = 0$ ) for the  $\text{HCCCN}\cdot\text{HCN}$  dimer is approximately 5 times larger than the corresponding contribution obtained for the  $\text{HCN}\cdot\text{HCCCN}$  dimer. Comparison of these theoretical values (Table 5) with the estimated experimental values for  $I_A$  (Table 2) shows excellent agreement for the smaller value of the  $\text{HCN}\cdot\text{HCCCN}$  dimer, whereas the larger value for the  $\text{HCCCN}\cdot\text{HCN}$  dimer is underestimated by a factor of 10. However, it is still significantly larger than the value for the  $\text{HCN}\cdot\text{HCCCN}$  dimer, by a factor of 5. So the difference between the helium moment of inertia contribution for two isomers predicted by the path integral calculations correctly reflects the large difference seen in the experimental spectra. Given the sensitivity of the nonsuperfluid density to the secondary saddle point region noted above, further refinement of the value of  $I_A$  for  $\text{HCCCN}\cdot\text{HCN}$  may be possible with generation of a higher level potential energy surface.

These theoretical values for the effective moments of inertia computed for both  $\text{HCCCN}\cdot\text{HCN}$  and  $\text{HCN}\cdot\text{HCCCN}$  are then used to make theoretical simulations of the rovibrational spectra

of the two binary complexes in the helium droplets. The theoretical spectra are shown as black lines at the bottom of Figures 1 and 2. In both cases, the  $P$ - and  $R$ -branches are in excellent agreement with the experimental data, reflecting the accuracy of the theoretical values of  $I_B$  for both dimers. Comparison between the theoretical simulated spectra in Figures 1 and 2 clearly shows the presence of a  $Q$ -branch for  $\text{HCCCN}\cdot\text{HCN}$  and the absence of a  $Q$ -branch for  $\text{HCN}\cdot\text{HCCCN}$ . As expected from the weaker accuracy of the theoretical values of  $I_A$ , the intensity of the  $Q$ -branch for the  $\text{HCCCN}\cdot\text{HCN}$  dimer is significantly lower than that observed in experiment. It is also less visible in the  $\nu_2$  spectrum than in the  $\nu_1$  spectrum because of the greater line width in the former spectrum (see above), to the extent that it appears only as a small feature in the  $\nu_2$  spectrum. Despite the underestimation of the absolute value of the moment of inertia  $\Delta I_A$  for  $\text{HCCCN}\cdot\text{HCN}$ , the infrared spectra simulated from the PIMC results are nevertheless clearly capable of distinguishing between the two dimers and correctly reproduce all key experimental spectroscopic features and differences. The underestimation of  $\Delta I_A$  for the  $\text{HCCCN}\cdot\text{HCN}$  dimer may be due to one or more of several factors, including the relatively small size of the cluster employed in the calculation, residual inaccuracies in the potential energy surface, and the different temperature ( $T = 0.31$  K) used in the calculations relative to the value  $T = 0.37$  K that is estimated for experimental measurements.<sup>25</sup> In this context, an analysis of the temperature dependence of the superfluid properties might provide further insight into the rotational

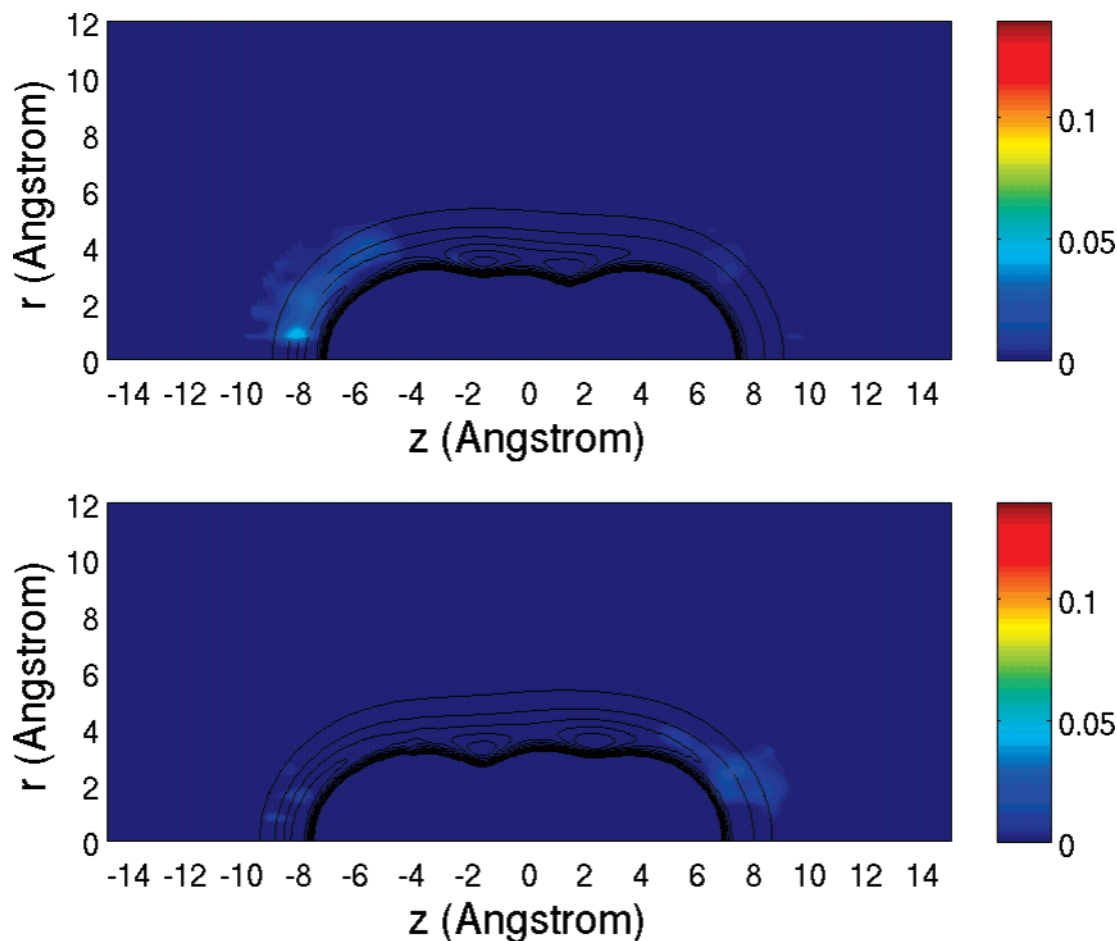


Figure 11.  $^4\text{He}$  parallel superfluid density for the HCCCN·HCN( $^4\text{He}$ ) $_N$  (top) and HCN·HCCCN( $^4\text{He}$ ) $_N$  (bottom) systems with  $N = 100$ .

TABLE 5:  $^4\text{He}$  Contribution to the Effective Moments of Inertia in  $\text{amu } \text{Å}^2$  for the HCCCN·HCN( $^4\text{He}$ ) $_N$  and HCN·HCCCN ( $^4\text{He}$ ) $_N$  Systems with  $N = 100$

	HCN·HCCCN	HCCCN·HCN
$A$	$20 \pm 10$	$110 \pm 10$
$\Delta I_B$	$760 \pm 20$	$1090 \pm 20$

dynamics of the HCCCN·HCN and HCN·HCCCN complexes in helium droplets, as well as into the nature of the nonsuperfluid density.

#### IV. Discussion and Conclusion

In this paper we have presented experimental and theoretical results for the rovibrational spectra of the HCCCN·HCN and HCN·HCCCN binary complexes in helium at low temperature. The experimental infrared spectrum of the  $\nu_1$  and  $\nu_2$  CH stretch bands of the linear HCCCN·HCN dimer show a prominent  $Q$ -branch, but no  $Q$ -branch is seen in the corresponding infrared spectrum of the HCN·HCCCN dimer in the helium droplets. The rotational constants  $B'$  and  $B''$  of both species are found to be renormalized by a factor of  $\sim 3$ , similar to what has been observed previously for many linear molecules. However, the observation of a  $Q$ -branch for a linear species, molecule or complex, in helium is generally anomalous. The marked difference between the two isomeric dimer complexes, with one showing and one not showing a  $Q$ -branch is even more unusual. We have analyzed this spectroscopic feature here as well as other differences between the two isomeric complexes in terms of the local distribution of superfluid and nonsuperfluid densities around the molecule, using finite temperature path integral

Monte Carlo calculations and potential energy surfaces from high level ab initio data. Calculations of structural and superfluid properties of both HCCCN·HCN( $^4\text{He}$ ) $_N$  and HCN·HCCCN( $^4\text{He}$ ) $_N$  clusters were made for  $N \leq 200$ . Overall, the  $^4\text{He}$  density distributions for the HCN·HCCCN( $^4\text{He}$ ) $_N$  system appear to be slightly more localized. This is particularly marked in the first solvation shell, reflecting a greater barrier to both motion and particle exchange along the molecular axes in this region. Detailed analysis of the potential energy surfaces, referring to the partial charge distribution on the dimer atoms shows that this can be explained by the different binding efficiency of helium to different locations along the molecular axis that maximizes its interaction with electron deficient regions of the dimers. Both isomers show pronounced perpendicular local nonsuperfluid densities, which are shown to result in reductions in the rotational constants consistent with the values derived from the experimental measurements. The HCCCN–HCN isomer shows larger perpendicular nonsuperfluid density, hence a larger  $\Delta I_B$  and a greater reduction in  $B$ , which results from the greater binding of helium to this isomer in the global and first secondary potential minima. For the parallel local nonsuperfluid density a significant difference is seen, with the HCN·HCCCN isomer showing only a very weak, diffuse distribution whereas the HCCCN·HCN isomer shows a marked parallel nonsuperfluid density near the acetylene end of the molecule. This is seen to correlate with small differences in both the densities and the angular variation of the potential energy surface and is rationalized here in terms of a resulting difficulty to make long permutation paths encircling the molecular axis for the HCCCN·HCN isomer. Full understanding of the difference in

parallel nonsuperfluid densities will require more detailed analysis of the permutation paths. Explicit calculation of the moments of inertia from these nonsuperfluid densities demonstrates that the measured differences in the rovibrational spectra of the HCCCN·HCN and HCN·HCCCN binary complexes in helium can be quantitatively accounted for by these local nonsuperfluid density distributions, with the significant parallel nonsuperfluid density of the HCCCN·HCN dimer resulting in a finite moment of inertia along the molecular axis for this species.

This study represents the first application of path integral Monte Carlo methods to detailed analysis of the phenomenon of anomalous  $Q$ -branch spectral features for linear molecules or complexes in helium. We expect that a more accurate potential energy surface might give a better estimate of the anomalous value of  $I_A$ , which the local nonsuperfluid density distribution calculated here would imply is sensitive to the potential energy surface around the acetylene moiety. Other factors such as temperature and cluster size may also play a role in determining the precise value of  $I_A$ . Nevertheless, the analysis with the current potential energy surface does provide a clear rationalization for the striking spectroscopic difference between the two isomers and for the origin of the  $Q$ -branch for the HCCCN·HCN isomer.

**Acknowledgment.** G.D. acknowledges the Graduate School at UNC—CH for a Royster Fellowship and the National Science Foundation for support under grant number CHE-99-87740. F.P. and K.B.W. thank the National Science Foundation for support under grant number CHE-01-07541.

## References and Notes

- (1) For a recent review see, e.g.: Toennies, J. P.; Vilesov, A. F. *Angew. Chem. Int. Ed.* **2004**, *43*, 2622.
- (2) Choi, M. Y.; Douberly, G. E.; Falconer, T. M.; Lewis, W. K.; Lindsay, C. M.; Merritt, J. M.; Stiles, P. L.; Miller, R. E. *Int. Rev. Phys. Chem.* **2006**, *25*, 15.
- (3) Nauta, K.; Miller, R. E. *J. Chem. Phys.* **2000**, *113*, 9466.
- (4) Nauta, K.; Miller, R. E. *Phys. Rev. Lett.* **1999**, *82*, 4480.
- (5) Nauta, K.; Miller, R. E. *J. Chem. Phys.* **2001**, *115*, 8384.
- (6) Grebenev, S.; Toennies, J. P.; Vilesov, A. F. *Science* **1998**, *279*, 2083.
- (7) Tang, J.; Xu, Y.; McKellar, A. R. W.; Jager, W. *Science* **2002**, *297*, 2030.
- (8) Xu, Y.; Jager, W. *J. Chem. Phys.* **2003**, *119*, 5457.
- (9) Tang, J.; McKellar, A. R. W. *J. Chem. Phys.* **2003**, *119*, 5467.
- (10) Paesani, F.; Viel, A.; Gianturco, F. A.; Whaley, K. B. *Phys. Rev. Lett.* **2003**, *90*, 73401.
- (11) Moroni, S.; Sarsa, A.; Fantoni, S.; Schmidt, K. E.; Baroni, S. *Phys. Rev. Lett.* **2003**, *90*, 143401.
- (12) Xu, Y.; Jager, W.; Tang, J.; McKellar, A. R. W. *Phys. Rev. Lett.* **2003**, *91*, 163401.
- (13) Tang, J.; McKellar, A. R. W.; Mezzacapo, F.; Moroni, S. *Phys. Rev. Lett.* **2004**, *92*, 145503.
- (14) Paesani, F.; Whaley, K. B. *J. Chem. Phys.* **2004**, *121*, 4180.
- (15) Grebenev, S.; Hartmann, M.; Havenith, M.; Sartakov, B.; Toennies, J. P.; Vilesov, A. F. *J. Chem. Phys.* **2000**, *112*, 4485.
- (16) Callegari, C.; Reinhard, I.; Lehmann, K. K.; Scoles, G.; Nauta, K.; Miller, R. E. *J. Chem. Phys.* **2000**, *113*, 4636.
- (17) Leggett, A. J. *Phys. Rev. Lett.* **1970**, *25*, 1543.
- (18) Kwon, Y.; Whaley, K. B. *Phys. Rev. Lett.* **1999**, *83*, 4108.
- (19) Kwon, Y.; Huang, P.; Patel, M. V.; Blume, D.; Whaley, K. B. *J. Chem. Phys.* **2000**, *113*, 6469.
- (20) Ceperley, D. M. *Rev. Mod. Phys.* **1995**, *67*, 279.
- (21) Paesani, F.; Kwon, Y.; Whaley, K. B. *Phys. Rev. Lett.* **2005**, *94*, 153401.
- (22) K. Y.; Paesani, F.; Whaley, K. B. *Phys. Rev. B* **2006**, *74*, 174522.
- (23) Draeger, E. W.; Ceperley, D. M. *Phys. Rev. Lett.* **2003**, *90*, 065301.
- (24) Brink, D. M.; Stringari, S. *Z. Phys. D* **1990**, *15*, 257.
- (25) Hartmann, M.; Miller, R. E.; Toennies, J. P.; Vilesov, A. F. *Phys. Rev. Lett.* **1995**, *75*, 1566.
- (26) Boys, S. F.; Bernardi, F. *Mol. Phys.* **1970**, *19*, 553.
- (27) Werner, H. J.; Knowles, P. J.; Almlöf, J.; Amos, R. D.; Berning, A.; Deegan, M. J. O.; Eckert, F.; Elbert, S. T.; Hampel, C.; Lindh, R.; et al. MOLPRO version 2002.1 (2002).
- (28) Aziz, R. A.; McCourt, F. R. W.; Wong, C. C. K. *Mol. Phys.* **1987**, *61*, 1487.
- (29) Feynman, R. P. *Phys. Rev.* **1953**, *91*, 1291.
- (30) Huang, P.; Kwon, Y.; Whaley, K. B. In *Quantum Fluids in Confinement*; Krotscheck, E., Navarro, J., Eds.; World Scientific: Singapore, 2002; Vol. 4, physics/0204089.
- (31) Paesani, F.; Whaley, K. B. *J. Chem. Phys.* **2004**, *121*, 5293.
- (32) Zillich, R. E.; Paesani, F.; Kwon, Y.; Whaley, K. B. *J. Chem. Phys.* **2005**, *123*, 114301.
- (33) Goffe, W. L.; Ferrier, G. D.; Rogers, J. J. *Econometrics* **1994**, *60*, 65.
- (34) Ceperley, D. M.; Pollock, E. L. *Phys. Rev. Lett.* **1986**, *56*, 351.
- (35) Nauta, K.; Miller, R. E. *J. Chem. Phys.* **1999**, *111*, 3426.
- (36) Yang, X.; Kerstel, E. R. T.; Scoles, G. *J. Chem. Phys.* **1993**, *98*, 2727.
- (37) Yang, X.; Kerstel, E. R. T.; Scoles, G. *J. Chem. Phys.* **1993**, *99*, 760.
- (38) Miller, R. E. *Science* **1988**, *240*, 447.
- (39) Nauta, K.; Moore, D. T.; Miller, R. E. *Faraday Discuss.* **1999**, *113*, 261.
- (40) Douberly, G. E.; Merritt, J. M.; Miller, R. E. *J. Phys. Chem. A* **2007**, *111*, 7282–7291.
- (41) Nauta, K.; Miller, R. E. *Science* **1999**, *283*, 1895.
- (42) Nauta, K. Ph.D. thesis, 2000.
- (43) Grebenev, S.; Sartakov, B.; Toennies, J. P.; Vilesov, A. F. *Science* **2000**, *289*, 1532.
- (44) Topic, W. C.; Jager, W. *J. Chem. Phys.* **2005**, *123*, 064303.
- (45) Atkins, K. M.; Hutson, J. M. *J. Chem. Phys.* **1996**, *105*, 440.
- (46) Dong, F.; Miller, R. E. *J. Phys. Chem. A* **2004**, *108*, 2181.